ChemCatChem

Research Article
doi.org/10.1002/cctc.202500189

Chemistry Europe
European Chemical Societies Publishing

www.chemcatchem.org

Waste Carbon-Derived Lanthanum Ferrite-Based Photocatalysts for 2-Propanol and Acetaldehyde Degradation

F. Deganello,[a] E.I. García-López,*[b] N. Aoun,[b, c] M. Sbacchi,[d] and G. Marcì[e]

Perovskite oxides have demonstrated great potential in catalysis and photocatalysis due to their unique morphological properties such as specific surface area and shape of particles. The current study focuses on the fabrication, characterization, and photocatalytic activity of $LaFeO_3$ perovskite oxides (LF) prepared by solution combustion synthesis in the presence or in the absence of waste activated carbon (WAC). The materials were characterized for their structural, microstructural, textural and morphological properties, and their photocatalytic activity was tested in gas-solid regime using simulated solar and UV irradiation sources. Two model molecules, 2-propanol and acetaldehyde, were selected, and it was found that 2-propanol was strongly adsorbed on the material, while acetaldehyde showed a more modest adsorption in dark conditions. The photocatalytic results indicate that the activity depends both on the presence of WAC and on the type of irradiation used. The uncalcined nanocomposite powder (LF-WAC-NC), where WAC was mostly preserved, showed the best ability to degrade acetaldehyde under UV and even under solar irradiation, suggesting that the photocatalyst takes advantage of the wider range of energies provided by the broader solar light spectrum compared with the monochromatic LED. On the contrary, the calcined nanocomposite (LF-WAC-700) was less active probably due to the absence of carbon and the contemporary presence of high percentage of aluminosilicates that remain after the removal of carbon due to the heat treatment.

1. Introduction

Volatile organic compounds (VOCs) play a crucial role as pollutants since the photochemical processes, triggered by sunlight radiation, are primarily responsible for the atmospheric breakdown. Acetaldehyde and 2-propanol are two examples of VOCs that significantly contribute to air pollution. 2-propanol is frequently utilized as a solvent in domestic and industrial products, while acetaldehyde is commonly generated as a result of biomass and industrial combustion processes. The prolonged exposure to these substances has detrimental impacts on the environment and human health.[1] Several photocatalytic studies have been carried out using 2-propanol and acetaldehyde as model molecules to tune the parameters linked to the photocatalysts and the set-up of the photocatalytic system. 2-propanol has been extensively used as model substrate for the sake of comparison of the activity of different photocatalysts as it possesses a relatively simple structure undergoing oxidative degradation pathways mediated by reactive oxygen species, making it an ideal probe molecule for evaluating the efficiency of photocatalysts.[2–4] It is a well-established benchmark in photocatalytic studies, ensuring reproducibility and direct comparison. Acetaldehyde has been also used as model substance to test the ability of semiconductors as photocatalysts.[5] Acetaldehyde photolyzes and combines with OH radicals (•OH) in air to generate peroxyacetyl nitrate (PAN), which is recognized as irritating for the eyes and respiratory system.[6] According to the classification provided by companies to ECHA (European Chemicals Agency) in REACH (Registration, Evaluation and Authorization of Chemicals), acetaldehyde was identified as a substance which is suspected of causing cancer.[5]

Perovskite oxides possess electronic properties that make them suitable for various catalytic and photocatalytic applications, included the VOC abatement.[4,7,8] Besides, they can be widely applied in the field of physics, material science, life sciences and chemistry, due to their extraordinary versatility in the chemical composition and relative functional properties.[9]

Among them, $LaFeO_3$ perovskite oxide possesses many important features such as high catalytic activity, excellent electric conductivity, high-quality ferroelectric properties, and excellent thermochemical stability.[10,11] Moreover, it has gained increasing scientific attention for its tunable band gap, its compositional and structural flexibility, and its efficient sunlight

[a] F. Deganello
Institute of Nanostructured Materials, Italian National Research Council, Palermo 90146, Italy

[b] E. García-López, N. Aoun
Department of Biological, Chemical and Pharmaceutical Sciences and Technologies (STEBICEF), University of Palermo, Palermo 90128, Italy
E-mail: elisaisabel.garcialopez@unipa.it

[c] N. Aoun
Department of Chemistry, Faculty of Exact Sciences and Informatics, University of Jijel, Jijel 18000, Algeria

[d] M. Sbacchi
Department of Chemical and Pharmaceutical Sciences, INSTM UdR Trieste, University of Trieste, Via Licio Giorgieri 1, Trieste 34127, Italy

[e] G. Marcì
Department of Engineering, University of Palermo, Palermo 90128, Italy

Supporting information for this article is available on the WWW under https://doi.org/10.1002/cctc.202500189

absorption. The application of $LaFeO_3$ in photocatalytic systems has been reported in the literature.[12,13] $LaFeO_3$ enables the generation of reactive oxygen species (ROS) as •OH or superoxide anions ($O_2^{\bullet}$), which play a crucial role in the oxidative degradation of VOCs, especially acetaldehyde.[14] Significant efforts have been devoted to improving its photocatalytic activity by different strategies, such as lattice substitution with heteroatoms, decoration, or structure regulation, giving rise to an enhanced photocatalytic activity performance.[15] The combination of $LaFeO_3$ and carbon has been investigated in the literature for application in photocatalysis.[16–20] The good features of perovskites to be used in photocatalysis in terms of physico-chemical properties as charge carrier mobility, optical absorption, among others[7] can be improved by obtaining composites with various forms of carbon, such as graphite, graphene, carbon black, graphene quantum dots (GQDs), and carbon quantum dots (CQDs). The presence of carbon along with perovskites in the photocatalyst have demonstrated effectiveness. It is reported that the composites broaden the light absorption range and improve the charge separation and transfer while reducing recombination of the carriers.[21] A recent example was reported by Kadkhodayan et al. who have used a composite perovskite/activated carbon for the degradation of dyes and reduction of nitrate and CO_2[22] and for antibiotics degradation[23] evidencing an improved photocatalytic activity of the composite attributed to the prolonged lifespan of electrons and holes. Furthermore, the absorption ability of the activated carbon also enhances the activity of the photocatalyst[22] justified by the well-known exceptional qualities of activated carbon such a high surface area, high degree of porosity and adsorption properties.[24] It is also reported that the loading of Zn_2SnO_4 perovskite nanoparticles with activated carbon significantly enhance the composite electrochemical performance with respect to the bare perovskite; authors observe also that activated carbon boosts the photocatalytic activity of the composite on the degradation rate of dyes.[25] $LaFeO_3$/Graphene Oxide ($LaFeO_3$-GO) hybrids were synthesized to evaluate their phosphate adsorption performance from water, in a series of systematically designed adsorption experiments, indicating the superior adsorption capacity of $LaFeO_3$-GO (103.11 mg/g) compared to other hybrids.[26] In addition, mesoporous $LaFeO_3$/g-C_3N_4 Z-scheme heterojunctions (LFC) showed remarkably enhanced adsorption capacity and oxytetracycline (OTC) photocatalytic degradation.[27] Moreover, carbon-based composites have displayed the capacity to reduce recombination of the produced electron and hole carriers during photocatalytic reaction.[28] An ultrasonication method has been used to synthesize a composite of silver-doped lanthanum ferrite with carbon nanotubes (AgLaFeO$_3$@CNT) for degradation of organic effluents under visible light.[29] In another study, C spheres have been synthesized by a hydrothermal method with $C_6H_{12}O_6{\cdot}6H_2O$ as a C source and used to prepare C-$LaFeO_3$ composites able to photodegrade methylene blue solution (MB) under visible light with an efficiency of 97%.[30]

Waste carbon precursors have been also used in the literature to obtain $LaFeO_3$-carbon binary systems. For example, Aghashiri et al. reported that the adsorption capacity (toward Crystal Violet) of the activated carbon prepared from sugar beet residue, as an agricultural waste material, was enhanced by decorating its surface with $LaFeO_3$ nanoparticles.[31] Guo et al. produced carbon from polypyrrole-functionalized waste medical masks, which was used as a support to impregnate $LaFeO_3$ nitrate precursors and, after thermal treatment under inert gas, obtain perovskite-carbon composites for the photocatalytic degradation of tetracycline with peroxymonosulfate.[32] Solution combustion synthesis is a convenient and efficient methodology for the preparation of mixed oxides, and it allows introducing solid precursors and templates in the synthesis.[33] Porous carbons are rarely used as hard templates in solution combustion synthesis.

In this work, $LaFeO_3$-waste activated carbon (WAC) nanocomposite powders were prepared by a one-pot solution combustion synthesis, using citric acid as a fuel and WAC as hard template. A $LaFeO_3$ reference powder prepared without WAC was also obtained. Their structural, microstructural, textural and morphological features, their band gaps and their photocatalytic activity in gas-solid regime toward 2-propanol and acetaldehyde degradation were evaluated before and after thermal treatment at 700 °C for 5 h. The aim was to evaluate the effect of the WAC in enhancing the photocatalytic performance of the perovskite oxide and to confirm the concrete possibility of exploiting a carbon waste for a fast and efficient synthesis of a photocatalyst for VOC abatement.

2. Experimental Section

2.1. Preparation of Pristine $LaFeO_3$ and Its Nanocomposite with Waste Activated Carbon

$LaFeO_3$ and $LaFeO_3$-WAC nanocomposites were prepared by solution combustion synthesis from citric acid as a fuel, in the absence or in the presence of WAC, respectively. WAC was kindly received in the form of granules from a car body shop (Carrozzeria Pellerito Unipersonale s.r.l., Palermo, Italy) and manually grinded into powder with mortar and pestle before adding it to the combustion mixture. The various steps of the solution combustion synthesis procedure are shown in Figure 1. In detail, to obtain 2 g of perovskite, 3.568 g of $La(NO_3)_3{\cdot}6H_2O$ (Alfa Aesar, purity: ≥ 99.99%) and 3.328 g of $Fe(NO_3)_3{\cdot}9H_2O$ (Aldrich, purity: 99.9%) were weighted and dissolved with (300 mL) deionized water in a 3 L stainless steel beaker. Anhydrous citric acid (Alfa Aesar, purity: 99.5%), in the amount of 6.327 g, was then added as a reducer, complexing agent and soft microstructural template, with a citric acid-to-metal cations ratio of 2. The compound NH_4NO_3 (J.J.Parker, purity: 95%), in the amount of 14.576 g, was added as an additional oxidant to obtain a reducers-to-oxidizers of 1. pH was regulated to 6 by adding ammonia solution (Aldrich, 30 vol%). Finally, 7.909 g of WAC were added to the combustion mixture, that was mechanically stirred at 80 °C for about 1.5 h until the formation of a greenish-black gel. The temperature of the hot-plate was set to 350 °C (temperature at the bottom of the beaker was about 200 °C) to initiate the auto-combustion of the gel, which was entirely converted into powder. A K-type thermocouple (1.5 mm in diameter) was inserted at the center of the beaker, in contact with the bottom, to register the temperature/time profiles during combustion at a sampling velocity of 20 bits s^{-1}. The thermocouple was connected to a data logger (PICO technology) and a computer with Picolog software. The as-burned powder (LF-WAC-NC) was then calcined to 700 °C for 5 h (with a ramp of 10 °C/min) to obtain LF-WAC-700. The sample without WAC was prepared under identical conditions although in the absence of WAC and obtained

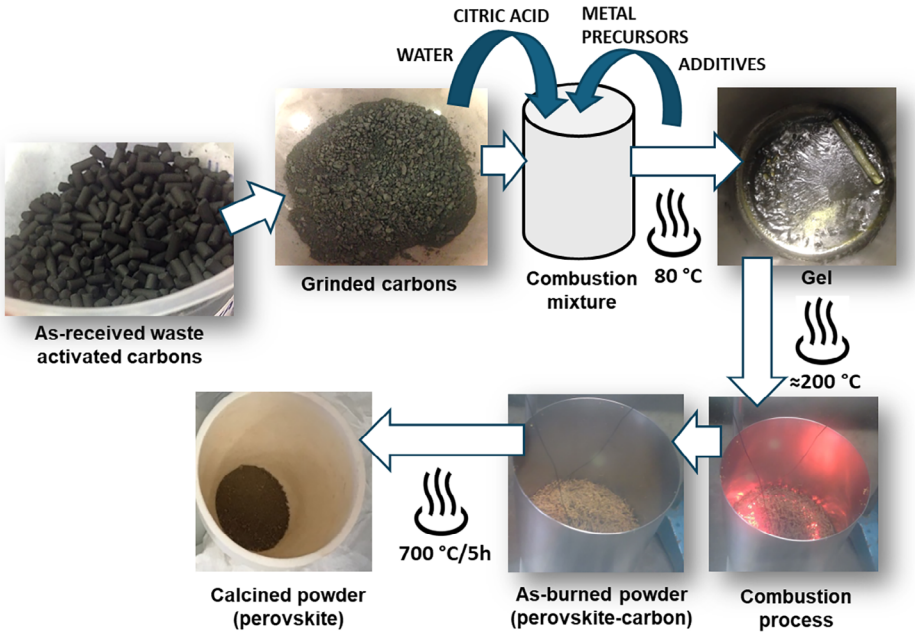

Figure 1. Schematic representation of the main steps for the synthesis of the perovskite-carbon nanocomposite.

both in the as-burned form (LF-NC) and after calcination at 700 °C (LF-700).

2.2. Physical-Chemical Characterization of the Perovskite and Nanocomposites with WAC

Structural properties of the powders were analyzed by X-ray diffraction and micro-Raman. X-ray diffraction measurements were performed on a Bruker-Siemens D5000 X-ray powder diffractometer with a Cu Kα radiation ($\lambda = 1.5418$ Å) operating at 40 kV and 30 mA in the 10–90° 2θ range, with a 0.03° 2θ step size and integration time of 20 s per step. The diffraction patterns were analyzed by Rietveld refinement using the GSAS-II software.[34] An 8th degree Chebyschev polynomials was chosen for the background. Scale factors, unit cell parameters, isotropic thermal motion parameters, sample displacement, microstrain, and crystallite size were considered as variable parameters. Micro-Raman spectra were acquired on pure powdered samples on a Renishaw using a Raman instrument equipped with an integrated microscope and a charge coupled device (CCD) camera. A He/Ne laser operating at $\lambda = 632.8$ nm was used as the exciting source.

Specific surface area (Brunauer–Emmett–Teller's method) and porosity were determined by N_2 adsorption/desorption measurements at −196 °C, using ASAP 2020 Plus (Version 1.03) after a pre-treatment under vacuum at 250 °C (heated at 10 °C min^{-1}) for 1 h prior to the measurements.

Scanning electron microscopy (SEM) was performed by using a FEI Quanta 200 ESEM microscope, operating at 20 kV on specimens upon which a thin layer of gold had been evaporated. An electron microprobe used in energy dispersive mode (EDX) was employed to obtain information on the actual atom content present in the samples.

Diffuse reflectance spectroscopy (DRS) of the solids was performed by a Shimadzu UV-2401 PC. The spectrum was recorded in the range of 200 to 800 nm at room temperature with $BaSO_4$ as the reference sample. The spectra of the samples were carried out by using mixtures of the photocatalyst with $BaSO_4$ in a mass ratio of 0.050:1.

2.3. Photocatalytic Experiments

The photocatalytic experiments were carried out in gas-solid regime by a cylindrical Pyrex batch photoreactor (diameter 42 mm, height 18 mm) of 25 mL. The powder (100 mg) was distributed at the bottom of the reactor and the inner atmosphere of the closed photoreactor was saturated with a continuous flow of O_2 (20 mL min^{-1}) for 30 min. After that, 2 µL of liquid 2-propanol (about 1.0 mM) or acetaldehyde (approximately 1.5 mM) were injected into the photoreactor. The details on the employed set-up are described elsewhere[7,8] where also 2-propanol was used as model molecule for the evaluation of the photocatalytic activity of $LaFeO_3$ based perovskites. Irradiation was initiated after reaching steady state conditions, which occurred after approximately 30–150 min (depending on the catalyst used) of dark stabilization. The photoreactor was irradiated from the top using two different systems, namely a UV-LED IRIS 40 with an irradiation peak centered at 365 nm and a SOLARBOX apparatus (CO.FO.ME.GRA srl) equipped with a 1500 W high pressure Xenon lamp that simulates solar light. The photon flow measured in the 315–400 nm region by a UVX Digital radiometer and reaching the reactor was 630 or 14 W m^{-2} for the UV-LED and SolarBox, respectively. The irradiated surface of the photoreactor was 1380 mm^2. The photocatalytic runs lasted two or 5 h under UV-LED or SolarBox irradiation, respectively and they were carried out in triplicate to verify their reproducibility.

To analyze the reacting fluid, 250 µL of gas was withdrawn from the reactor using a gas-tight syringe. The concentrations of the substrate and its reaction intermediates were determined using a Shimadzu 2010 gas chromatograph (GC) equipped with a Phenomenex Zebron Wax-plus and a FID detector with He as carrier gas. The amount of CO_2 was analyzed using a HP 6890 Series GC equipped with a packed column GC 60/80 Carboxen-1000 and a TCD. The same experimental conditions as the photoreactivity studies were used for the blank reactivity investigations, but no catalyst, or oxygen, or light were present; since no reactivity was observed under these conditions, it was concluded that the model molecules degradation process require the simultaneous presence of O_2, solid photocatalyst and light to occur.

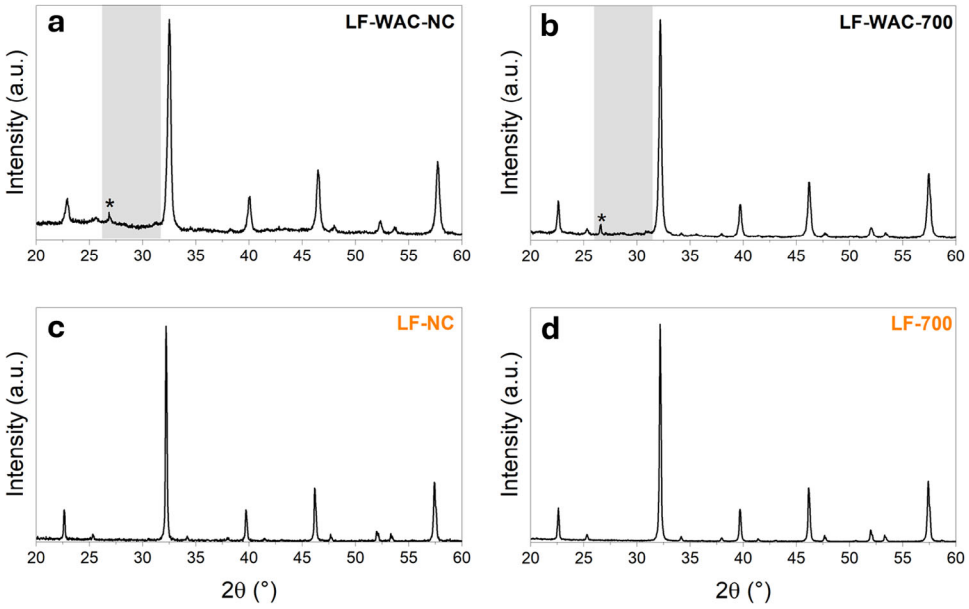

Figure 2. XRD patterns of LF and LF-WAC powdered samples, before (a,c) and after (b,d) the thermal treatment at 700 °C. The asterisk indicates the main peak of a graphite-like carbon. The grey region indicates formation of secondary phases and/or pronounced background in the LF-WAC powders. The intensity scales are different for LF and LF-WAC patterns and have been selected for each pattern to maximize the intensity in each graph.

3. Results and Discussion

In Figure S1, the two temperature-time profiles registered during the combustion synthesis of LF and LF-WAC samples are shown. The combustion process in the presence of WAC was as intense as in its absence, indicating that WAC did not block the combustion wave as other hard templates, like for example silica.[35]

3.1. Physical-Chemical Characterization of the Perovskite and Nanocomposites with WAC

The XRD patterns of the four powdered samples are reported in Figure 2, whereas the Rietveld refinement results are shown in Table 1, and the graphical fittings are reported in Figure S2a–d. The orthorhombic (Pnma) $LaFeO_3$ perovskite-type phase is clearly identified in all the patterns, including those of the as-burned powders, indicating that the $LaFeO_3$ perovskite oxide phase was already generated before the thermal treatment, due to the high temperature reached during the combustion process (Figure S1). The absence of peaks belonging to secondary phases in both the patterns of the reference samples, LF-NC and LF-700, indicates that the orthorhombic perovskite was the unique crystalline phase, whereas in the LF-WAC-NC and LF-WAC-700 samples a peak of crystalline graphitic carbon (*) and other small peaks due to aluminosilicate impurities are visible (Figure 2), in agreement with the EDX results that support the presence of Al and Si, particularly in the calcined powder. Aluminum and silicon have been also detected in the original WAC, and are kept in the LF-WAC powders, since they represent the inorganic ashes of WAC. Moreover, LF-WAC-NC contains nanostructured carbon, as evidenced by the prominent background signal (Figure S2c). The amount of nanostructured carbon is 84 ± 4 wt%, as estimated by Rietveld refinement, by considering the nanostructured carbon phase in the fitting. This value is in agreement with the nominal amount of WAC introduced in the synthesis (80 wt% WAC and 20 wt% of $LaFeO_3$). The heat treatment at 700 °C totally burns the carbon off and the large peak of nanostructured carbon disappears (Figure S2d) leaving a purer and more crystalline perovskite phase. It is worth to notice that the $LaFeO_3$ formed in the presence of WAC has much smaller crystal sizes but much greater microstrain (Table 1), indicating a clear microstructural templating effect of WAC. In addition, $LaFeO_3$ phase generated in the presence of WAC has a smaller cell volume (Table 1), suggesting that WAC may have a structural templating impact that lasts over the heat treatment. The structural templating impact of WAC could be due to various factors. The high microstrain may indicate a structural tension due to the fact that the perovskite oxide crystallite is forced to grow onto the WAC surface, although it can be due as well to a compositional tension due to doping of the perovskite structure. In fact, we cannot exclude that the slight volume contraction could also be due to the presence of a minor percentage of impurities coming from the original WAC (see discussion on EDX below). For example, Aluminum[36] which has, as Al^{3+}, a smaller ionic radius than Fe^{3+} and can replace Fe-site of the $LaFeO_3$, inducing a volume contraction of about 1 $Å^3$ for each 5 mol% Al introduced at the Fe-site, indicating that, if Al effectively replaced the Fe-site, its percentage would be less than 0.04 mol% Al. Another impurity that could decrease the cell volume is Calcium. Ca can replace the La-site and induce a decrease of the cell volume, due to the increase in the percentage of Fe^{4+} which has a smaller ionic radius than Fe^{3+}.[37] However, the volume contraction due to the Ca introduction at the La-site is of about 2.7 $Å^3$ for each 10 mol% Ca introduced, whereas the volume decreases of only 0.7 $Å^3$, sug-

Table 1. Rietveld analysis results: $LaFeO_3$ cell parameters, crystal size and microstrain with corresponding standard deviations. In the last column reliability factors (Rw and GOF) are reported. The space group of the perovskite is P n m a.

Sample name	Unit cell lenghts (Å) and Volume (Å^3)	Crystal size (nm)	Microstrain (no unit)	Reliability factors (%)
LF-NC	5.5659 ± 0.0001 7.8528 ± 0.0002 5.5537 ± 0.0002 242.71 ± 0.01	116 ± 1	325*	Rw = 9.18 GOF = 1.34
LF-700	5.5650 ± 0.0001 7.8528 ± 0.0002 5.5534 ± 0.0001 242.69 ± 0.01	115 ± 2	325 ± 76	Rw = 8.33 GOF = 1.22
LF-WAC-NC	5.554 ± 0.001 7.851 ± 0.004 5.550 ± 0.003 242.01 ± 0.04	45.00 ± 0.5	2709*	Rw = 9.00 GOF = 1.47
LF-WAC-700	5.5585 ± 0.0007 7.8434 ± 0.001 5.5495 ± 0.0008 241.95 ± 0.03	62.00 ± 0.2	2709 ± 246	Rw = 9.37 GOF = 1.41

* Microstrain and UISO values for the un-calcined samples were fixed at the values obtained from the fitting of the calcined samples.

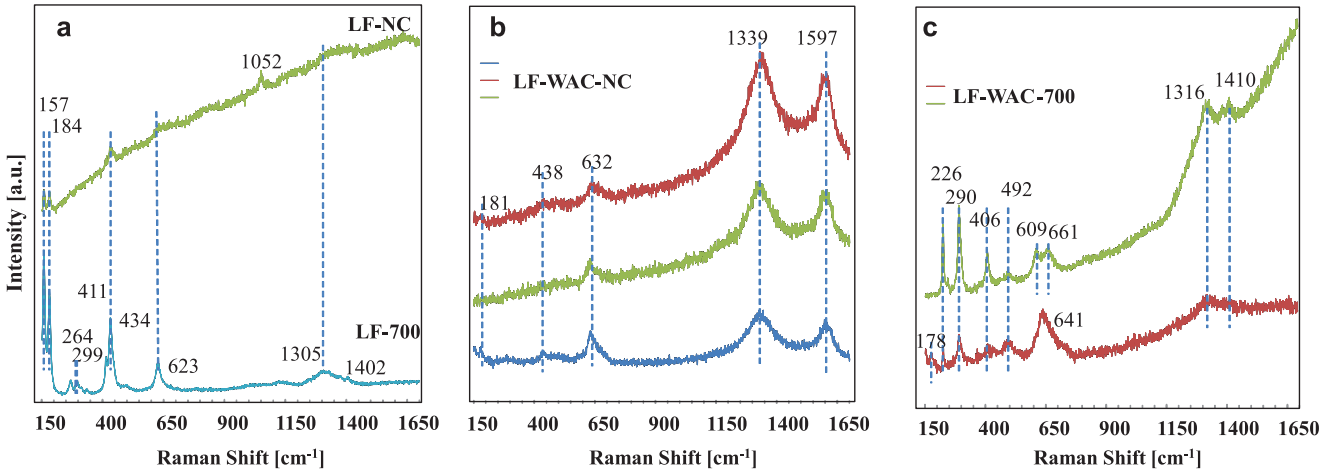

Figure 3. Raman spectra of (a) pristine $LaFeO_3$ calcined (LF-700) and not calcined (LF-NC), (b) not calcined $LaFeO_3$-WAC nanocomposite (LF-WAC-NC), and (c) $LaFeO_3$-WAC nanocomposite calcined at 700 °C (LF-WAC-700), both analyzed on different spots on the sample.

gesting that the Ca amount should be very low, of about 3 mol%. Similar considerations can be applied for Na doping at the La-site,[38] where a volume contraction of 0.4 Å^3 each 10 mol% Na introduced in the perovskite oxide, although in this case the calculated percentage of dopant reaches 20 mol%, suggesting that Na could have been effectively entered the $LaFeO_3$ structure. Regarding Si doping, no information is available in the literature and therefore is less probable. Sulfur could replace the O-site of the perovskite, although the effect would be an expansion of the cell volume,[39] and thus sulfur doping is not very much probable.

Micro-Raman spectroscopy is a very useful tool to study structural properties of composite materials and to determine the phases present and the homogeneity of the structure. The Raman modes analyzed in the reference perovskite samples (LF-NC and LF-700) are shown in Figure 3a, and they are fully consistent with those previously observed in literature for the $LaFeO_3$ orthorhombic Pbnm structure. The band at 150 and 184 cm^{-1}, the couple at 264, 299 cm^{-1}, that centered at 430 cm^{-1} and the transition at 623 cm^{-1} are in good agreement with those observed before for the same kind of materials.[40–42] The thermal treatment gives rise to better order in the perovskite system, so influencing the quality of the transitions. Raman analyses carried out on different spots of the sample confirm the homogeneity of the specimen, as evidenced by the spectra reported in Figure 3b. In the Raman spectra of the powders prepared with WAC, in addition to the characteristic peaks of the $LaFeO_3$ (see Figure 3b,c), two peaks corresponding to the D and G bands are present, attributed to the graphitic material. These transitions are reported to be located typically at 1350 and 1580 cm^{-1}.[43,44] The D band arises from the limitations in the graphite domain size, induced by grain boundaries or imperfections, such as substitu-

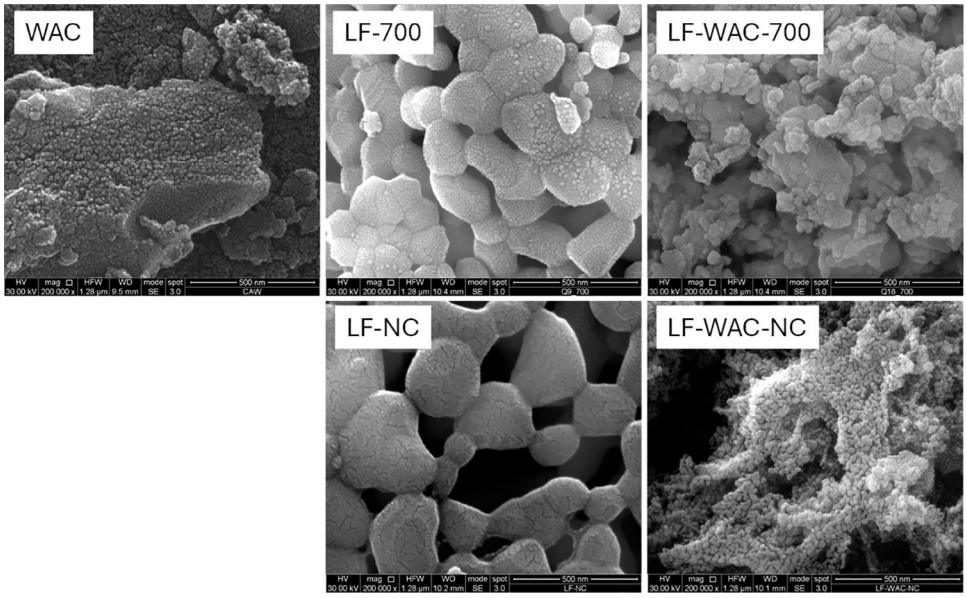

Figure 4. SEM micrographs of WAC, calcined (LF-700 and LF-WAC-700) and uncalcined (LF-NC and LF-WAC-NC) powders.

Table 2. Some textural properties of the powdered samples determined from N_2 adsorption experiments: specific surface area (S.S.A.), cumulative pore volume and mean pore size.

Sample	S.S.A. (m^2 g^{-1})	BJH desorption cumulative volume of pores (cm^3 g^{-1})	Mean pore size (nm)
WAC	272 ± 2	0.072	3.54
LF-NC	5.08 ± 0.07	0.012	4–50*
LF-700	6.02 ± 0.02	0.032	4–20*
LF-WAC-NC	524 ± 3	0.116	3.89
LF-WAC-700	13.16 ± 0.04	0.076	26.29

* Very low porosity and no clear peaks.

tional N atoms, sp^3 carbon, or impurities and is active only in the presence of materials containing a certain degree of disorder. In the sample LF-WAC-NC (see Figure 3b), the D transition is located at 1339 cm^{-1}, as previously observed in similar specimens.[44] The G band at around 1597 cm^{-1} corresponds to the symmetric E2g mode in graphite-like materials arises from the stretching of the C-C bond and is common to all sp^2 carbon systems. The D-mode is caused by disordered structure of graphene. Calcined LF-WAC-700 sample presented a certain degree of inhomogeneity due to the waste origin of the carbon material, however the bands attributed to the LF are present and can be well assigned to the orthorhombic form. Localized vibrational modes of the impurities can interact with the extended phonon modes of graphene resulting in the observed widening and shifting of the peaks, notable those assigned to the carbon material are not evident.

The morphology of waste activated carbon (WAC) shown in Figure 4 appears to be made up of large agglomerates of nanoparticles whose size ranged between 3–5 nm. Moreover, WAC possesses a porous structure, which is responsible for its adsorptive capabilities. Interestingly, the spaces between the nanoparticles have the size of ca. 3–5 nm in agreement with the size of the pores measured by N_2 adsorption-desorption isotherms (see Table 2). In the micrograph of the LF-700 sample it is shown that the particles presented a more defined and crystalline morphology structure than those of WAC, with smoother surfaces. Moreover, they appear more homogeneous and with a more compact morphology. The large and uniform particles indicate that the perovskite phase was successfully formed, as evidenced also by the high crystallinity observed by the XRD.

Interestingly, the morphology of the as-burned powder (LF-NC), as shown in Figure 4, is very similar to that of the calcined material (LF-700), indicating that this thermal treatment, with a dwell temperature very close to the maximum temperature in the temperature/time profile (Figure S1), does not give rise to further sintering phenomena, in agreement with XRD data on crystal size. As far as the composite LF-WAC-NC is concerned, the micrograph in Figure 4 shows that the resulting composite has a very similar appearance to the starting WAC. Therefore, it is possible to assume that the WAC has completely covered the resulting composite, or, more probably, that nanostructured perovskite crystallites have been grown onto the WAC surface, being affected by the microstructural templating action of WAC. In facts, the perovskite oxide is formed in the presence of waste activated carbon during the combustion process in the synthe-

sis and crystal size of the perovskite oxide in Table 1 indicates its nanostructured nature. On the contrary, the morphology of the LF-WAC-700 sample shows a significant variation with respect to the constituent parts (WAC and LF-700). In fact, during the heat treatment at 700 °C, the WAC initially present in the LF-WAC-NC sample was burned (see XRD analysis), allowing the perovskite oxide crystallites to sinter. However, from the analysis of Figure 4, LF-WAC-700 particles are larger than those of WAC, but smaller than those of LF-700. Moreover, they appear to be an intricate structure, possibly as a result of the interaction between the perovskite and activated carbon during the growth of the perovskite oxide crystals on the WAC surface. The roughness is more noticeable than in the pristine perovskite LF-700, suggesting that the porous structure of the activated carbon may have influenced the formation of the final nanocomposite. The activated carbon (WAC) appears to have served as a microstructural template during the synthesis, influencing the shape of the composite before and even after calcination. The perovskite phase and activated carbon were successfully integrated during the combustion synthesis, producing a material with improved features, as an increased surface area that could enhance catalytic performance or adsorption capability. However, the post thermal treatment of 700 °C reduced the photocatalytic activity of LF-WAC-700 sample (see Section 3.2). Indeed, as observed by XRD analysis, carbon disappeared in this latter sample leaving, as revealed by EDX analysis, significant percentage of Al (ca. 5 at. %) and Si (ca. 7 at. %) and lower amount of Na, S and Ca deriving from the aluminosilicates present in the WAC used for the catalyst preparation. Indeed, these species were observed in both LF-WAC-NC and bare WAC, although only in traces.

The N_2 adsorption-desorption isotherms for LF-NC, WAC and LF-WAC-NC are reported in Figure 5a, whereas the corresponding pore size distribution is shown in Figure 5b. The LF-WAC-NC isotherm displays a typical Type IV isotherm, indicating that the material is mesoporous. The presence of a hysteresis loop indicates that capillary condensation is taking place in the mesopores. It is worth noticing that the WAC isotherm exhibits a comparable pattern, albeit with a little reduced capacity for adsorption, suggesting a similar mesoporous architecture and confirming the microstructural templating effect of WAC during the crystal growth. The LF-NC sample's much decreased adsorption capability suggests a more limited adsorption capacity across the pressure range, less accessible pores and a denser material microstructure. Following thermal treatment (Figure 5c,d) there is a shift toward larger pores or reduced total porosity, resulting in a decrease in mesoporosity. The adsorption capacity is strongly reduced both for LF and LF-WAC samples, indicating that a pore collapse or surface area reduction has occurred during sintering. However, LF-WAC-700 maintained a slightly higher porosity than LF-700 (Figure 5d). These results could be critical in assessing the impact of thermal treatment on the material's textural properties, especially when considering surface area and pore structure for applications like catalysis or adsorption.

As a support of the previous discussion, Table 2 reports a comparison among the textural properties of the samples investigated. The LF-WAC-NC powder has the highest surface area, and this is probably due to the copresence with WAC that was not burned during the combustion process. However, the nanocomposite powder has a surface area that is even higher than the original WAC. This could be due to the further contribution of the low crystal size of the perovskite phase (Table 1). It is worth noticing that the mean pore size of LF-WAC-NC is almost the same as that of WAC, indicating that WAC is not very much subjected to transformation during the combustion process.

The N_2-adsorption results agree as well with the SEM results of Figure 4, where WAC has the lowest particle size and LF-WAC-700 has a smaller particle size than LF-700. Probably, the textural characteristics of the calcined sample were impacted by the transformation of WAC into graphitic carbon and aluminosilicates during thermal treatment at 700 °C.

Diffuse reflectance spectra of all of the photocatalyst along with the Tauc plots, determined only for the bare perovskite materials (LF-NC and LF-700) are reported in Figure 6. The uncalcined perovskite LF-NC exhibits slightly more absorbance (lower reflectance) in the visible part of the spectra with respect to the LF-700 sample, indicating a higher ability to absorb visible light, possibly due to slight structural differences and/or defects. The low light reflectance ability of the composites with WAC, LF-WAC-NC and LF-WAC-700, evidenced in Figure 6, indicates a strong light absorption as a result of the presence of the activated carbon in their structures. This insight was observed before in composites with TiO_2 or ZnO and activated carbon.[45,46]

With the aim of estimating the optical band gap of the semiconductors, the diffuse reflectance spectra collected for the pristine perovskites, LF-NC and LF-700, were firstly used to obtain the Kubelka–Munk function, $F(R_\infty)$, that represents the equivalent of absorbance spectra. For the composites containing WAC the use of this function to calculate the absorption is controversial due to the difficulties associated to rationalize the electronic transitions occurring in the composites, that could vary upon the interfacial electronic interactions between the carbon and the perovskite, and the strong light absorbing nature of the carbon matrix.[47]

Consequently, the band-gap values of the two pristine perovskite samples were estimated by extrapolating a linear fitting in the Tauc plot corresponding to the function $([F(R_\infty)\bullet h\nu]^2$ versus the $h\nu$ values, assuming a direct transition[48–51] as shown in Figure 6. It is worth to mention that, the determination of the optical band gap of $LaFeO_3$ is not univocal. For instance, according to Ab initio studies, $LaFeO_3$ fundamental gap is indirect (~3.4 eV);[52] however, the optical absorption, measured by DRS and then Tauc plot, i.e., the optical spectroscopy observes a direct-allowed transition at lower energies (~2.5–2.6 eV), depending on the crystallite size.[53] This explains why despite its indirect nature, $LaFeO_3$ absorbs visible light and often behaves like a narrow-gap semiconductor in photocatalytic applications.

For both prepared materials, an estimated band gap of 2.5 eV has been measured in the Tauc plot, the fitted value. This band gap is in agreement with those reported in literature for $LaFeO_3$ showing electronic transitions in the range 2.0 to 2.5 eV, depending on the preparation conditions.[54]

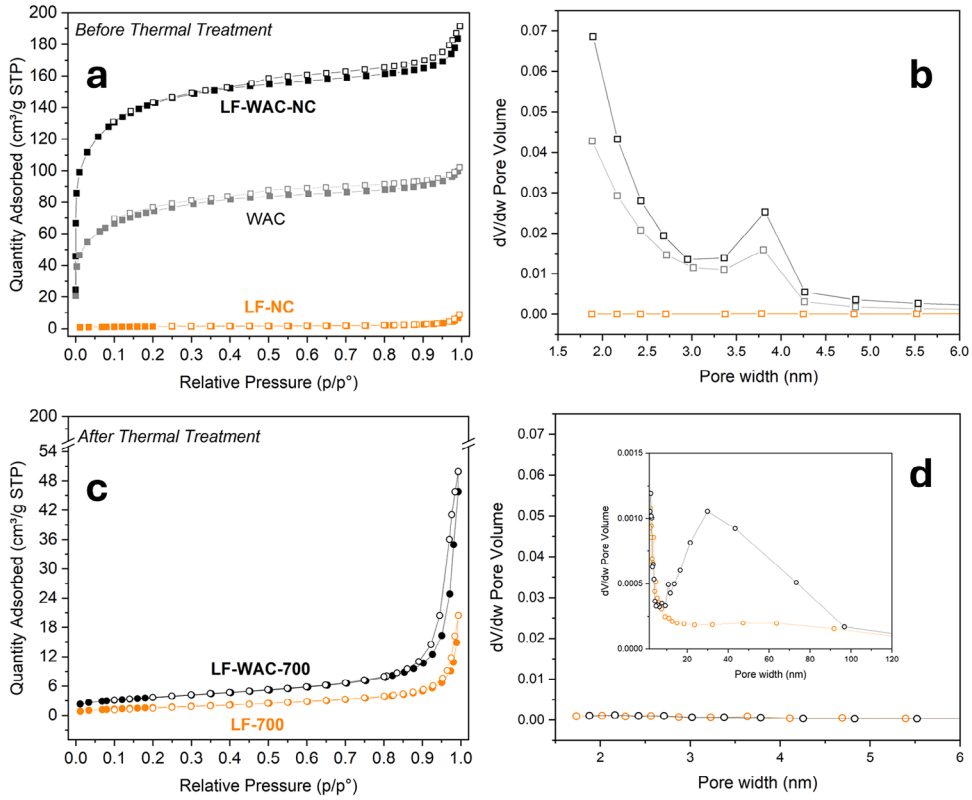

Figure 5. N_2 adsorption/desorption isotherms and pore size distribution (a, b) before and (c, d) after thermal treatment, for LF and LF-WAC samples and for the WAC powder.

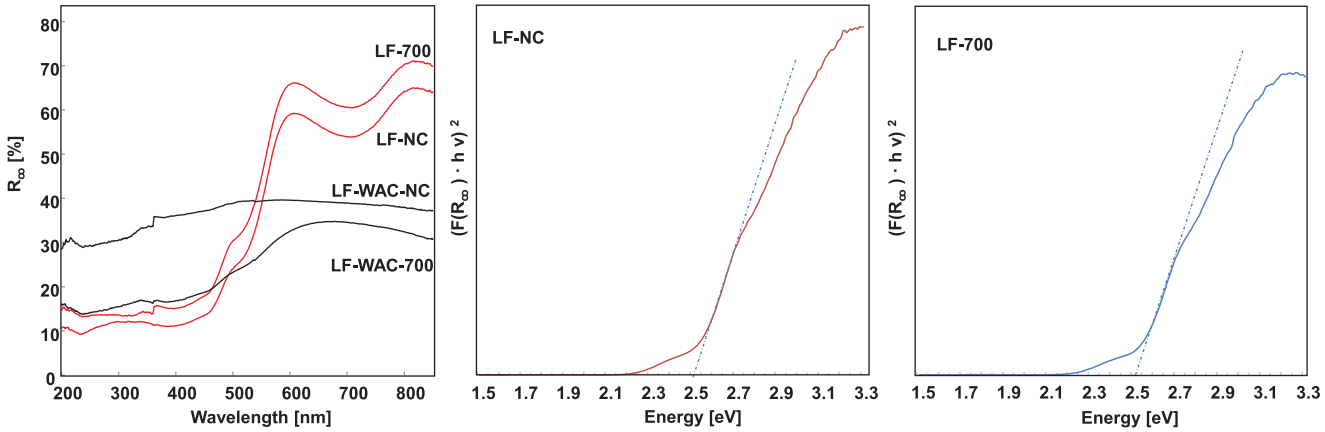

Figure 6. DRS of the prepared bare and composite photocatalysts and Tauc plots of the bare perovskite semiconductors.

3.2. Photocatalytic Activity of the Pristine Perovskite and Perovskite-WAC Nanocomposites

Dark experiments are carried out to evaluate the capability of the prepared materials to adsorb 2-propanol or acetaldehyde. The adsorption results in the dark lead to the conclusion that the 2-propanol is almost completely adsorbed by all the solids, as reported in Table 3. Also, acetaldehyde is adsorbed but to a lower extent (see Table 3). The decreasing in the acetaldehyde concentration due to the adsorption on the photocatalyst surface in dark conditions, is shown in Figure 7. Interestingly, 2-propanol strongly adsorbs even on the perovskite alone, in fact both in the presence of WAC and in its absence, there is always an almost total adsorption. On the other hand, in the case of acetaldehyde, it adsorbs slightly on the perovskite and its adsorption increases when WAC is present. According to the results reported in Figure 7, the adsorption of acetaldehyde, which was evaluated during 150 min in the dark, is modest for the LF-NC sample and slightly higher in the presence of the calcined perovskite (LF-700), whereas it is enhanced by the presence of the WAC in the composite.

The adsorption and the conversion of the acetaldehyde in the presence of the pristine $LaFeO_3$ perovskite and the composite materials are summarized in Table 3.

Table 3. Adsorption of the model molecules in dark conditions as well as acetaldehyde conversion, the CO_2 concentration at the end of the runs and pseudo-first-order kinetic constant (k_{obs}) for the acetaldehyde degradation by using the two different irradiation Solarbox or UV-LED.

Sample	2-Propanol adsorption (%)	Acetaldehyde adsorption (%)	Conversion (%)			CO_2 concentration (mM)		k_{obs} $\times 10^3$ (min^{-1})	
			Solar 2 h	Solar 5 h	LED	Solar 5 h	LED	Solar	LED
LF-NC	97	28	73	93	79	2.6	2.3	9.2	10.3
LF-700	96	40	79	99	83	2.8	2.4	9.7	11.5
LF-WAC-NC	98	77	85	100	100	2.7	2.8	13.0	20.2
LF-WAC-700	97	58	71	87	83	2.5	2.4	5.8	9.6

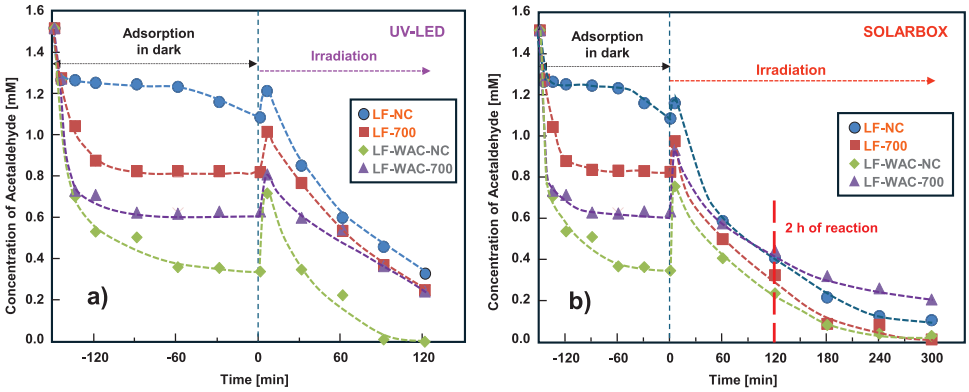

Figure 7. Acetaldehyde concentration evolution in the dark and during the reactivity experiment carried out under (a) UV-LED or (b) solar light simulated (SOLARBOX) irradiation. The values of the acetaldehyde concentration reported in the figures are the average obtained in three different runs. In any case the oscillations of the values were in the range of ± 5%.

After the adsorption step, the irradiation of the photocatalytic reactor started. The irradiation causes the formation of partial oxidation products of both 2-propanol and acetaldehyde. However, the strong ability of the solids to absorb 2-propanol and acetone, its oxidation product, hindered the possibility to study the photocatalytic activity of the materials by using this molecule as the substrate to be degraded. On the contrary, it was possible to study the photooxidation of acetaldehyde and consequently Figure 7 reports only the evolution of the concentration of this molecule versus the irradiation time (under both UV-LED and SOLARBOX irradiation) in the presence of all the photocatalyst prepared.

As far as the oxidation of acetaldehyde under both UV-LED and Solar-simulated irradiation is concerned, all the nanomaterials show photocatalytic activities, and LF-WAC-NC yield the best oxidation efficiency (see Figure 7a,b).

From the perusal of Figure 7a,b, it is evident that during the first instants of irradiation, both under UV light and simulated sunlight, part of the 2-propanol is desorbed from the catalysts. However, after this stage in which the concentration of acetaldehyde in the gas phase is increased, a new decrease of its concentration versus the irradiation time is observed. In Table 3 are reported, for each catalyst, the percentage of acetaldehyde disappeared from the gas phase after 2 h of irradiation for both kind of systems and also after 5 h of irradiation in the case of the runs carried out in the SOLARBOX. Interestingly, during the degradation of acetaldehyde only traces of acetic acid were observed, probably because the latter remains more strongly adsorbed on the catalysts. Consequently, in order to understand whether the disappearance of acetaldehyde was due to its further adsorption on the catalyst or to its partial oxidation to acetic acid, which remained adsorbed on the catalyst, or to its total degradation to CO_2, the concentration of CO_2 in gas phase was measured the at the end of each test and these values are reported in Table 3.

The concentration of CO_2 measured at the end of each run was close, only slightly lower, to the stoichiometric value. This insight indicates that the disappearance of acetaldehyde is due to its degradation.

The disappearance of acetaldehyde versus the irradiation time for all the runs follows an exponential curve indicating a pseudo-first-order kinetic. Consequently, the pseudo-first-order kinetic constants were calculated and their values, for each catalyst, are collected in Table 3.

It is interesting to note that the various catalysts have a very similar photocatalytic activity each to the other with the exception of the LF-WAC-NC material (the only one that contains carbon) which is always the most performant. This fact indicates that the presence of carbon in this material is beneficial, probably due to the ability of carbon to reversibly adsorb acetaldehyde. In fact, the carbon present in this material, adsorbing acetaldehyde, works as a reservoir of this species and it is able to rapidly refill the photocatalytic sites of the perovskite adjacent to it. In practice, carbon concentrates acetaldehyde in proximity to the catalytic sites, increasing the photocatalytic activity. The photocatalytic activity of LF-WAC-700 was signifi-

cantly lower than that of LF-WAC-NC, probably not only due to the absence of carbon in the former but also to the presence of significant percentages of other species (Al and Si) contained in the aluminosilicates present in the WAC used in the preparation of the material (see Section 3.1) which can work as recombination centres of the hole-electron pairs. In fact, the presence of inorganic impurities such as Al and Si and others in waste activated carbon (WAC), particularly in the form of aluminosilicates after calcination, appears to negatively affect the photocatalytic degradation of acetaldehyde. These impurities may partially block the active sites of $LaFeO_3$ and scatter incident light, thereby reducing the effective photon absorption and surface reactivity. Additionally, aluminosilicates are generally photoinactive and may alter the acid-base surface properties, decreasing the adsorption affinity for acetaldehyde. In contrast, the uncalcined nanocomposite (LF-WAC-NC), where carbon is preserved and aluminosilicate exposure is minimized, shows improved photocatalytic performance, likely due to enhanced light harvesting, better charge separation, and more favourable surface interactions with the target pollutant.

By comparing the results reported in Figure 7a with those reported in Figure 7b and also in Table 3, it can be observed that the performances of the catalysts under UV-LED are only slightly higher with respect to those carried out under simulated solar light, at least in the case of the catalysts that do not contain carbon. Consequently, it can be hypothesized that the higher amount of UV photons emitted by the LED compared to that of the solar simulator could amplify the effect of the presence of carbon discussed above leading to a faster complete degradation of the substrate by using LF-WAC-NC catalyst.

4. Conclusions

$LaFeO_3$ were prepared via solution combustion synthesis in the presence and in the absence of waste activated carbon (WAC) with or without further thermal treatment. All the obtained nanomaterials were used as heterogeneous photocatalysts for the 2-propanol and acetaldehyde oxidation in gas-solid regime by irradiating the system with simulated solar light or with an UV-LED. The model molecules, acetaldehyde and 2-propanol, were remarkably adsorbed by all the photocatalysts. However, 2-propanol and its intermediates remained adsorbed onto the photocatalyst surface, hindering further investigation on its reactivity. On the other hand, the higher surface area of the nanocomposite and the improved dispersion of the perovskite oxide, produced one-pot with WAC, clearly favored the adsorption of acetaldehyde without blocking the active sites. During the initial steps of the photocatalytic reaction, acetaldehyde experienced photo/thermal desorption and analyses of the final oxidation product included CO_2. The most active photocatalyst was LF-WAC-NC, the $LaFeO_3$ prepared in the presence of WAC and without further thermal treatment, that, under both the Solarbox and UV-LED irradiation, gave a conversion of acetaldehyde of ca. 100%. For this material, some combined characteristics, like the reduced crystal size, increased specific area (ca. 525 $m^2\ g^{-1}$), and cooperation with WAC particles in the adsorption/photodegradation processes, could justify the highest activity observed among the other materials tested. The role of WAC is thus double, as a microstructural template and functional additive to the perovskite oxide photocatalyst.

Acknowledgments

F.D. thanks the CNR-ISMN technician Francesco Giordano for performing the XRD measurements. Dr. Valeria La Parola and the CNR-ISMN technician Nunzio Gallì are also acknowledged for performing the N_2 adsorption measurements. Dr. Rossana Gentile is greatly acknowledged for her collaboration in the synthesis of the powders.

Open access publishing facilitated by Universita degli Studi di Palermo, as part of the Wiley - CRUI-CARE agreement.

Conflict of Interests

The authors declare no conflict of interest.

Data Availability Statement

The data that support the findings of this study are available from the corresponding author upon reasonable request.

Keywords: Acetaldehyde · Activated carbon · $LaFeO_3$ · Perovskite · Photocatalysis · Solution combustion synthesis

[1] R. Atkinson, D. L. Baulch, R. A. Cox, R. F. Hampson Jr, J. A. Kerr, M. J. Rossi, J. Troe, *Phys. Chem. Ref. Data* **2000**, *2*, 167–266.
[2] E. I. García-López, G. Marcì, F. R. Pomilla, M. C. Paganini, C. Gionco, E. Giamello, L. Palmisano, *Catal. Today* **2018**, *313*, 100–105.
[3] E. I. García-López, G. Marcì, M. V. Dozzi, L. Palmisano, *Catal. Today* **2019**, *328*, 118–124.
[4] F. Parrino, E. García-López, G. Marcì, I. Natali-Sora, L. Armelao, *J. Alloys Comp.* **2016**, *682*, 686–694.
[5] B. Tryba, P. Rychtowski, A. Markowska-Szczupak, J. J. Przepiórski, *Catalysts* **2020**, *10*, 1464.
[6] B. J. Finlayson-Pitts, J. N. Pitts Jr, *Chemistry of the Upper and Lower Atmosphere: Theory, Experiments, and Applications*, Elsevier, Amsterdam, **1999**.
[7] R. Kumar, D. Kumar, P. E. Lokhande, V. Kadam, C. Jagtap, A. S. Vedapathak, K. Singh, Y. K. Mishra, A. Kaushik, *Coord. Chem. Rev.* **2025**, *34*, 216556.
[8] N. Aoun, E. I. García-López, H. Boucheloukh, M. Boulekroune, T. Sehili, G. Marcì, *J. Photochem. Photobiol. A* **2025**, *458*, 115930.
[9] M. Christy, S. Choi, J. Kwon, J. Jeong, U. Paik, T. Song, *Small Sci.* **2025**, *5*, 2400386.
[10] F. A. Fabian, P. P. Pedra, J. L. S. Filho, J. G. S. Duque, C. T. Meneses, *J. Magn. Magn. Mater.* **2015**, *379*, 80.
[11] E. Konysheva, J. T. S. Irvine, *Chem. Mater.* **2009**, *21*, 1514–1523.
[12] F. Mahmoudi, K. Saravanakumar, V. Maheskumar, L. K. Njaramba, Y. Yoon, C. M. Park, *J. Hazardous Mater.* **2022**, *436*, 129074.
[13] A. Bianco Prevot, D. Fabbri, E. Bernardini, F. Deganello, M. L. Tummino, G. Magnacca, in *Materials Science in Photocatalysis* (Eds: E.I. García-López, L. Palmisano), Elsevier, Amsterdam, **2021**, pp. 357–370.
[14] E. I. García-López, G. Marcì, B. Megna, F. Parisi, L. Armelao, A. Trovarelli, M. Boaro, L. Palmisano, *J. Catal.* **2015**, *321*, 13-22.

[15] E. García-López, G. Marcì, F. Puleo, V. La Parola, L. F. Liotta, *Appl. Catal. B* **2015**, *178*, 218–225.
[16] K. Wang, H. Niu, J. Chen, J. Song, C. Mao, S. Zhang, Y. Gao, *Appl. Surf. Sci.* **2017**, *404*, 138.
[17] R. D. Kumar, R. Thangappan, R. Jayavel, *J. Inorg. Organomet. Polym.* **2017**, *27*, 892–900.
[18] Y. Lu, Y. Dong, W. Liu, J. Liu, Q. Jin, L. Zheng, H. Lin, *Sep. Purif. Tech.* **2024**, *330*, 125336.
[19] L. Wei, Y. Zhang, C. Zhang, C. Yao, C. Ni, X. Li, *ACS Appl. Nano Mater.* **2023**, *6*, 13127–13136.
[20] P. Hao, Y. S. Rui, S. J. Zhang, B. Li, Z. Y. J. Wang, B. Liu, Z. Wang, X. Qiao, *ACS Omega* **2023**, *8*, 41744–41754.
[21] R. Soni, V. Soni, P. E. Lokhande, N. M. Mubarak, K. Singh, D. Kumar, S. Praveenkumar, R. Kumar, U. Rednam, R. Aepurui, K. Shanmugara, *Mater. Horiz.* **2025**, *12*, 3234–3266.
[22] H. Kadkhodayan, T. Alizadeh, *Mater. Today Chem.* **2022**, *26*, 101034.
[23] H. Kadkhodayan, T. Alizadeh, *J. Phys. Chem. Solids* **2023**, *183*, 111620.
[24] P. Zhang, H. Zhu, S. Dai, *ChemCatChem* **2015**, *7*, 2788–2805.
[25] S. Dinesh, N. Thirugnanam, M. Anandan, S. Barathan, N. Anandhan *J. Mater. Sci.: Mater. Electron.* **2016**, *27*, 12786–12795.
[26] J. Rauf, M. A. Inam, R. Iftikhar, H. Amjad, D. Nabi, W. Usmani, *J. Water Process Eng.* **2024**, *67*, 106158.
[27] K. Xu, X. Yang, L. Ruan, S. Qi, J. Liu, K. Liu, S. Pan, G. Feng, Z. Dai, X. Yang, R. Li, J. Feng, *Catalysts* **2020**, *10*, 301.
[28] E. I. García-López, P. Lo Meo, A. Di Vincenzo, L. Palmisano, G. Marcì, *Catal. Today* **2023**, *413–415*, 113965.
[29] N. Alfryyan, A. Irshad, S. Altaf, B. Basha, M. S. Al-Buriahi, Z. A. Alrowaili, H. Sabeeh, M. I. Din, *J. Korean Ceram. Soc.* **2024**, *61*, 115–125.
[30] S. Li, M. Li, M. Xu, X. Li, K. Gao, *Sustainability* **2023**, *15*, 715.
[31] A. Aghashiri, S. Hashemian, F. K. Fotooh, *J. Mol. Struc.* **2022**, *1260*, 132822.
[32] L. Guo, J. Zhi, Y. Yang, Y. Jiang, S. Chen, Y. Jia, X. Li, *Colloids Surf. A* **2024**, *703*, 135336.
[33] F. Deganello, A. K. Tyagi, *Prog. Crystal Grow Charact. Mater.* **2018**, *64*, 23-61.
[34] B. H. Toby, R. B. Von Dreele, *J. Appl. Cryst.* **2013**, *46*, 544-549.
[35] F. Deganello, M. L. Testa, V. La Parola, A. Longo, A. C. Tavares, *J. Mater. Chem. A* **2014**, *2*, 8438–8447.
[36] J. Vidhya, R. Gayathri, G. V. S. S. Sarma, K. Banupriya, S. Yuvaraj, L. Rajadurai, M. Sundararajan, *Ceram. Int.* **2025**, in press.
[37] G. Pecchi, M. G. Jiliberto, A. Buljan, E. J. Delgado, *Solid State Ionics* **2011**, *187*, 27–32.
[38] M. B. Bellakki, V. Manivannan, P. McCurdy, S. Kohli, *J. Rare Earths* **2009**, *27*, 691–697.
[39] S. Li, X. Zhu, K. Gao, *J. Chin. Chem. Soc.* **2024**, *71*, 348–357.
[40] M. Popa, J. Frantti, M. Kakihana, *Solid State Ionics* **2002**, *154–155*, 437-445.
[41] S. Chanda, S. Saha, A. Dutta, B. Irfan, R. Chatterjee, T. Sinha, *J. Alloys Compd.* **2015**, *649*, 1260-1266.
[42] A. S. Mahapatra, A. Mitra, A. Mallick, M. Ghosh, P. Chakrabarti, *Mater. Lett.* **2016**, *169*, 160.
[43] A. C. Ferrari, J. Robertson, *Phys. Rev. B* **2000**, *61*, 14095-14107.
[44] H. Xueqiu, L. Xianfeng, N. Baisheng, S. Dazhao, *Fuel* **2017**, *206*, 555.
[45] J. Matos, E. I. García-López, L. Palmisano, A. García, G. Marcì, *Applied Catal. B* **2010**, *99*, 170–180.
[46] J. C. Escamilla, J. Hidalgo-Carrillo, J. Martín-Gómez, R. C. Estévez-Toledano, V. Montes, D. Cosano, F. J. Urbano, A. Marinas, *Materials* **2020**, *13*, 3800.
[47] G. D. Gesesse, A. Gomis-Berenguer, M. F. Barthe, C. O. Ania, *J. Photochem. Photobiol. A* **2020**, *398*, 112622.
[48] A. Kumar, K. Sharma, M. Thakur, D. Pathania, A. Sharma, *J. Environ. Chem. Eng.* **2022**, *10*, 108098.
[49] S. Sudheer Khan, J. P. Steffy, A. T. Alfagham, A. M. Elgorban, *J. Water Proc. Eng.* **2025**, *71*, 107174.
[50] M. A. Wahba, M. M. G. Abdelkader, E. H. El-Mossalamy, *Mater. Chem. Phys.* **2025**, *341*, 130916.
[51] P. García-Muñoz, F. Fresno, J. Ivanez, D. Robert, N. Keller, *J. Hazar. Mater.* **2020**, *400*, 123099.
[52] M. D. Scafetta, A. M. Cordi, J. M. Rondinelli, S. J. May, *J. Phys.: Condens. Matter.* **2014**, *26*, 505502.
[53] R. Köferstein, L. Jäger, S. G. Ebbinghaus, *Solid State Ionics* **2013**, *1–5*, 249–250.
[54] A. Mishra, N. Priyadarshini, S. Mansingh, K. Parida, *Adv. Colloid Interf. Sci.* **2024**, *333*, 103300.

Manuscript received: February 4, 2025
Revised manuscript received: June 24, 2025
Accepted manuscript online: July 4, 2025
Version of record online: ■■, ■■